

# Effect of the Sliding Velocity on the Size and Amount of Airborne Wear Particles Generated from Dry Sliding Wheel–Rail Contacts

Hailong Liu<sup>1</sup> · Yingying Cha<sup>2</sup> · Ulf Olofsson<sup>2</sup> · Lage Tord Ingemar Jonsson<sup>1,3</sup> · Pär Göran Jönsson<sup>1</sup>

Received: 20 May 2016 / Accepted: 5 July 2016 / Published online: 19 July 2016  
© The Author(s) 2016. This article is published with open access at Springerlink.com

**Abstract** A set of frictional experiments have been conducted on a pin-on-disk apparatus to investigate the effect of the sliding velocity on airborne wear particles generated from dry sliding wheel–rail contacts. The size and the amount of generated particles were acquired by using particle counter instruments during the whole test period. After the completion of tests, the morphology and chemical compositions of pin worn surfaces and collected particles were analyzed by using scanning electron microscopy combined with an energy-dispersive X-ray analysis system. The results show that the total particle number concentration increases dramatically with an increased sliding velocity from 0.1 to 3.4 m/s. Moreover, the fine and ultrafine particles ( $<1\ \mu\text{m}$ ) dominates the particle generation mode in the case of a high sliding velocity (1.2 and 3.4 m/s). The contact temperature variation is observed to be closely related to the size mode of the particle generation. In addition, the sliding velocity is found to influence the active wear. Correspondingly, an oxidative wear is identified as the predominant wear mechanisms for cases with high sliding velocities (1.2 and 3.4 m/s). This produces a substantial number of iron oxide-containing particles ( $<1\ \mu\text{m}$ ) and reduces the wear rate to a relative low level (the wear rate for a 3.4 m/s sliding velocity is 4.5 % of that for a 0.4 m/s sliding velocity).

**Keywords** Dry sliding contact · Airborne wear particles · Temperature · Oxidative wear · Wheel rail

## 1 Introduction

A large variety of loading conditions and contact geometries exist between railway wheels and rails due to many different rail and wheel profiles, rail cant and curve radii and railway vehicles running on specific networks. Contact mainly occurs at a wheel tread–rail head in tangent tracks and a wheel flange–rail gauge corner contact in curves. The latter one is usually more severe which leads to greater wear being seen. The wheel–rail contact is a rolling contact with sliding, and the sliding takes place on both tangent and curved track. Furthermore, it increases in curves with a relative sliding velocity peak when braking in a narrow curve. A study by Lewis and Olofsson [1] based on GENSYS simulations and laboratory tests to create a wear map of wheel–rail contact conditions indicates that the rail gauge–wheel flange contact will experience a severe to a catastrophic wear. As a result, the severe and catastrophic wear of a wheel–rail sliding contact have been speculated to contribute to the high particulate matter levels detected in subway environments [2–4].

Thus, the sliding wear of the wheel–rail contact can be catastrophic. This can result in that the accompanying emitted airborne particles will increase the PM levels in subway stations. On the other hand, the relevant wear test data are limited. Specifically, experimental tests have been conducted to simulate the sliding wheel–rail contacts in terms of the identification of the wear mode and the characteristics of generated airborne wear particles [5–7]. A relative narrow selection of contact conditions has been considered in all these studies. However, the field operation

✉ Hailong Liu  
hailongl@kth.se

<sup>1</sup> Department of Materials Science and Engineering, KTH-Royal Institute of Technology, 100 44 Stockholm, Sweden

<sup>2</sup> Department of Machine Design, KTH-Royal Institute of Technology, 100 44 Stockholm, Sweden

<sup>3</sup> Division of CBRN Defence and Security, FOI, Swedish Defence Research Agency, 901 82 Umeå, Sweden

conditions can be more complex and beyond the reported region in some cases, such as for a heavy braking or acceleration in a sharp curved track [8]. Also, it can be expected that a high sliding velocity can yield a large amount of frictional heat. This, in turn, will elevate the contact temperature at the wheel–rail contact interface. Such temperature variations could trigger a thermal or chemical process and therefore result in an increased generation of sub-micrometer ( $<1\ \mu\text{m}$ ) particles [9]. Also, a high contact temperature enables the formation of oxide layers in the wheel rail contact and influences the wear performance [10, 11]. However, few test data are known to verify that statement. In the view of the human health, there is evidence that some potential adverse health effects can be caused by an inhalation of submicron particles during a longer period [12–14]. Thus, it is of importance to investigate the generation mechanism of airborne particles, and in particular submicron particles, from the wear process of a sliding wheel–rail contact for different sliding velocities.

The objective of this study is to examine the effect of sliding velocities on the wear behavior, the contact temperature and the particle emission in a dry sliding wheel–rail contact. Furthermore, to identify the different wear mechanisms involved in the formation of airborne wear particles.

## 2 Experimental Methodology

### 2.1 Test Setup

The test setup was previously presented by Olofsson et al. [15], and it is used to simulate the pure sliding part of the rolling sliding wheel–rail contact. Especially for simulating cases where extreme sliding occurs such as in very tight curves, this test setup has been proven to provide useful information [16]. Although twin-disk test setup has been considered as a better choice to simulate both rolling and sliding in a wheel–rail contact, it has to perform a complicated redesign when dealing with a case of high sliding velocity. A schematic diagram of the test stand is illustrated in Fig. 1. The tests were performed on a pin-on-disk tribometer with a horizontal rotating disk and a dead-weight-loaded pin. The tribometer is capable to work under controlled conditions of a constant normal force up to 100 N and a programmed rotational speed of up to 3000 rpm. The particle measurement system is connected to a ventilated chamber. During experiments, the fan (B) brings the air from the room (A) into the chamber (G) via a flow measurement system (C), a filter (D) and through the air inlet (F). The cleanliness of the injected air is guaranteed by the filter. Also, flexible tubes (E) are used

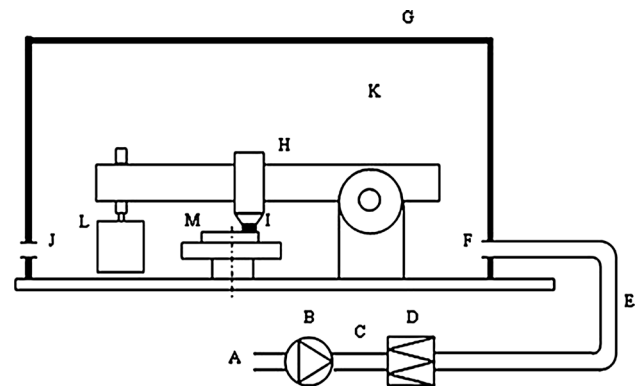


**Fig. 1** Schematic illustration of the test equipment, (A) room air; (B) fan; (C) flow rate measurement; (D) filter; (E) flexible tube; (F) inlet for clean air, measurement point; (G) closed chamber; (H) pin-on-disk machine; (I) pin sample; (J) air outlet, measurement points; (K) air inside chamber; (L) dead weight; and (M) rotating disk sample

to connect the fan, flow rate measurement system, filter and chamber. The air inside the chamber is well mixed (K) due to the complex geometry of the pin-on-disk machine body (H). The emitted airborne wear particles from the contact between the pin sample (I) and the rotating disk sample (M) are transported by the air flow to the air outlet (J), where the sampling points for counting particles are located. All connections between the chamber and the measurement system are sealed to prevent a leakage, which in principle might influence the measurements. However, the effect of a leakage on the tests can be neglected due to that the air pressure inside the tubes is far higher than outside the tubes.

### 2.2 Particle Counter Instruments

Two particle counting instruments were used to register the concentration and the size distribution of the generated particles. The first instrument is a Fast Mobility Particle Sizer<sup>TM</sup> (FMPS<sup>TM</sup>, model 3091, TSI Inc., MN, USA) spectrometer, where the electrical mobility detection technique is adopted to measure the number concentration of sub-micrometer aerosol particles over a wide range from 5.6 to 560 nm using 32 channels. The FMPS instrument works at a high sample flow rate of 10 l/min, which assists to minimize the particle sampling losses due to diffusion [17]. During the measurements, the time resolution was set to be one second. The second counter is an optical particle sizer (OPS, TSI Inc., MN, USA) spectrometer. A laser beam is employed in the OPS to size and count the particles. The OPS instrument possesses a wide range of identifiable aerosol sizes (0.3–10  $\mu\text{m}$ ). Furthermore, one extra instrument was used to sample and collect particles on size-separated filters. The electrical low-pressure impactor

(ELPI+™, Dekati Ltd., Finland) is used to collect particles. The operating principle of the ELPI+ is that the particles are firstly charged by a corona changer and then classified by using a low-pressure cascade impactor combined with an electrical detection by using a multi-channel electrometer. The ELPI+ consists of 14 stages in total, which enables a collection of particles in the aerodynamic diameter range from 6 nm to 10 μm. During the tests, the generated particles were collected separately according to their different sizes on greased aluminum filters during these 14 impactor stages. Thereafter, the collected particles on the aluminum filters were analyzed chemically after the completion of the experiments.

### 2.3 Test Specimen

Four pairs of pins and disks were used for the tests. The pins and disks material were cut from commercial used UIC60 900A rail and R7 wheel materials, respectively. The pins were manufactured into specimens with a cylindrical shape (diameter 10 mm) to be fixed in the pin holder. The head of pins was a half-spherical shape. During an experiment, the pin head was in contact with the disks. The height of each pin was 15 mm. Also, the disks were manufactured into cylindrical plates with a diameter of 105 mm and a thickness of 9 mm. All the specimens were polished to get a smooth enough surface topography. Table 1 shows the detailed information of the samples including dimensions as well as surface roughness and hardness data. The chemical compositions of the test specimens were determined by using an IR detection system and by using optical emission spectrometry (OES), as listed in Table 2.

### 2.4 Test Procedure

Before the tests, all specimens were cleaned ultrasonically for 20 min in a methanol solution. Subsequently, a set of tests were run on the pin-on-disk tribometer. A constant normal load of 5 N was used to guarantee a contact pressure to 800 Mpa. This value was calculated by using the Hertzian contact theory [18] for an assumed initial contact of a sphere and a plane between the pin and the disk. Four different sliding velocities were examined. The selected sliding velocities and contact pressure represent three typical contact situations of the sliding wheel–rail

contact, a rail head–wheel tread contact (0.1 m/s), a rail gauge–wheel flange contact (0.4 m/s) and an extreme contact corresponding to a braking in sharp curves (1.2 and 3.4 m/s). The detailed test plan is listed in Table 3, and each test was repeated twice.

### 2.5 Measurement of Wear Rate and Average Contact Temperature

The wear rate was estimated as the difference in the weight of the test specimens (pins) before and after the test, divided by the sliding distance. The variation of the wear rate for each two tests was evaluated by using a mean value and a standard deviation. Overall, the measurement uncertainty for the wear rate was less than 5 %. Moreover, the average contact temperature was measured by inserting a thermocouple wire into the head of the pins instead of at the actual contact interface. This is due to the difficulty to perform such a measurement. The tip of the thermal couple was placed at a 1 mm distance from the contact interface of the pin and the disk. All tests were performed in the chamber under a constant temperature ( $22^{\circ}\text{C} \pm 2$ ) and a clean particle concentration background.

### 2.6 Morphology Analysis of Worn Surfaces and Collected Particles

The collected particles with small sizes (stage 2 and stage 4) were analyzed by using a JEOL7800F field emission scanning electron microscope (FE-SEM, JEOL, Ltd. Japan) combined with an energy-dispersive X-ray microanalysis system (EDS) to observe the morphologies and to analyze the elemental contents. Before the analysis, the samples were gold coated with a thickness of  $\approx 10$  nm by using sputtering. The collected larger particles (stage 6 and stage 8) and the worn surfaces of pins were directly analyzed by using a Hitachi S-3700N scanning electron microscope (SEM, Hitachi, Ltd. Japan) combined with EDS.

## 3 Results

The results of the particle number concentration, size distribution, wear rate of the tested pins and the contact temperature measured under selected different sliding velocities are illustrated in this section. Herein, the particle

**Table 1** Characteristics of test specimens

Specimen	Material	Dimension (mm)	Surface roughness Ra (μm)	Hardness (HV)
Pin	UIC60 900A rail	Diameter 10 Height 15	0.3–0.6	300
Disk	R7 wheel	Diameter 105 Thickness 9	0.3–0.6	400

**Table 2** Chemical composition of test specimens (wt%)

	C	Si	Mn	Cr	Ni	Cu	Fe
UIC60 900A rail	0.55	0.37	0.88	0.21	0.1	0.19	Balanced
R7 wheel	0.66	0.45	1.27	1.07	0.05	0.054	Balanced

**Table 3** Test conditions for pin-on-disk tests

Sliding velocity (m/s)	Time (min)	Normal load (N)	Contact pressure (MPa)
0.1	20	5	800
0.4	20	5	800
1.2	20	5	800
3.4	20	5	800

sizes were classified into the following three fractions: coarse (1–10  $\mu\text{m}$ ), fine (0.1–1  $\mu\text{m}$ ) and ultrafine (<0.1  $\mu\text{m}$ ) [19]. In addition, the morphological and elemental analyses of the pin worn surfaces and collected particles are presented in this section.

### 3.1 Particle Number Concentration and Size Distribution

Figure 2 shows the representative results of the particle number concentration (PNC) over the test time and the corresponding sliding distance, measured by the OPS for

four different sliding velocities. It should be noted that the scale of the PNC value differs in each graph, namely  $7 \times 10^3$ ,  $3.5 \times 10^4$ ,  $3.5 \times 10^4$  and  $1.4 \times 10^5$  in Fig. 2a–d, respectively. It can be seen that the total number concentration of the generated airborne particles increases with an increased sliding velocity. To be specific, Fig. 2a shows a quite low average PNC value ( $<3 \times 10^2/l$ ) for a 0.1 m/s sliding velocity. However, increased average PNC values can be observed for higher sliding velocities (0.4, 1.2 and 3.4 m/s). For the test using a 3.4 m/s sliding velocity (Fig. 2d), the PNC value starts with a rapid increase at the initial stage of the measurement. Thereafter, it is kept at a

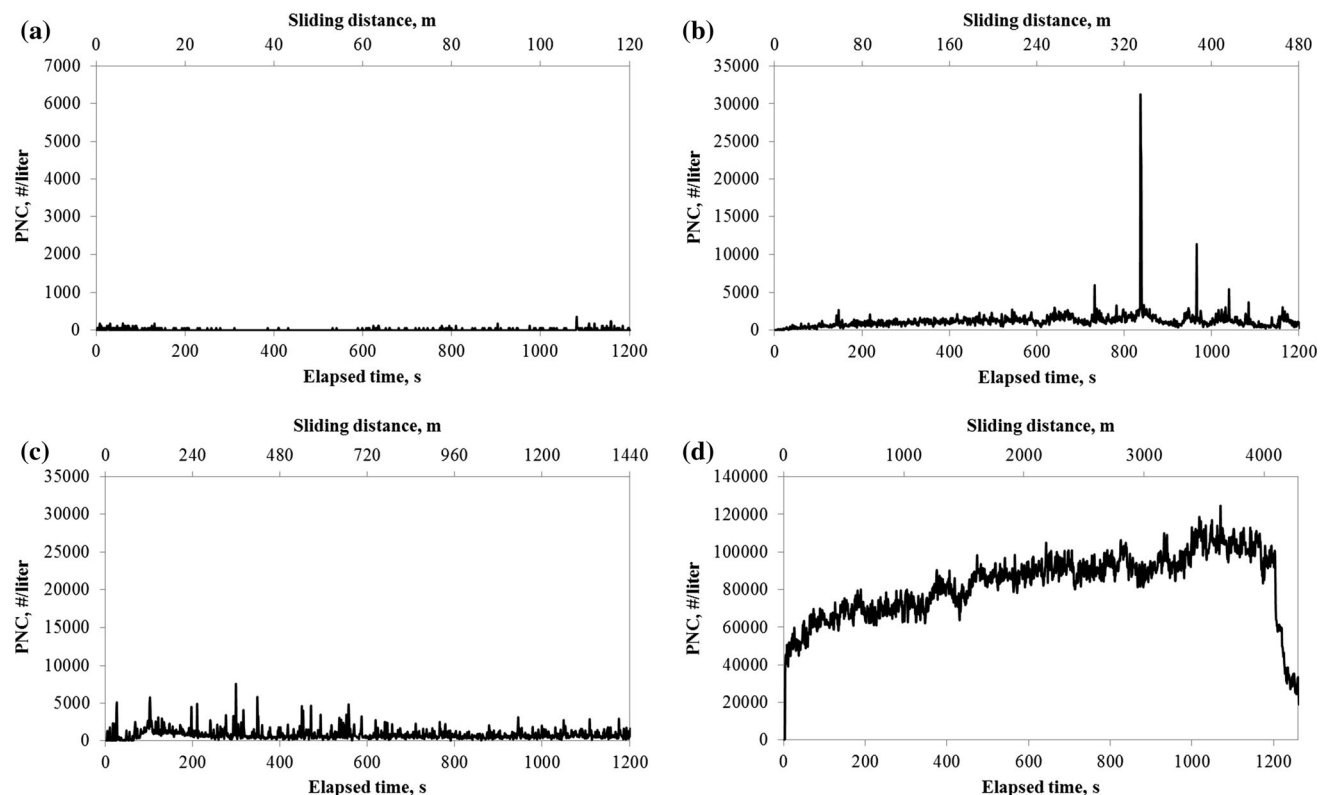


**Fig. 2** Particle number concentration measured by the OPS instrument for different sliding velocities, **a** 0.1 m/s, **b** 0.4 m/s, **c** 1.2 m/s and **d** 3.4 m/s

relative low level. After the running-in stage has been completed, the PNC value rises sharply to a level of around  $6 \times 10^4/l$ . Then, it increases slightly and gradually over the remaining part of the test period. Differently to what is found in Fig. 2a, c, d, several considerable peaks with a relative high PNC value together with a fluctuating PNC value are observed in Fig. 2b. The corresponding normalized particle size distributions during the whole test period for the different sliding velocities are illustrated in Fig. 3. It indicates that the generated particles at the four sliding velocities contain a dominating fraction of fine particles (smaller than  $1 \mu\text{m}$ ). It is also seen that a proportion of coarse particles is observed at low sliding velocities (0.1 and 0.4 m/s). Moreover, it is worth noting that more than 90 % of the detected particles are smaller than  $1 \mu\text{m}$  for the high sliding velocity cases of 1.2 and 3.4 m/s. In order to enhance the understanding on the fine fractions for tests with high sliding velocities, the FMPS measurement results were analyzed, in a manner as shown in Fig. 4. The total PNC was found to reach a very high level of millions per liters. However, the PNC variation differs from the tests using sliding velocities of 1.2 and 3.4 m/s. For the case of a 1.2 m/s sliding velocity, the PNC value rises dramatically to a considerable high peak value of  $3.75 \times 10^6/l$  at the beginning stage. Then, it drops to a relative low level corresponding to an average value of  $1 \times 10^5/l$  during the remaining part of the test. The difference in the results for a 3.4 m/s velocity is that the PNC value experiences a sharp rise from 0 to  $6 \times 10^5/l$  during the initial sliding stage. Then, it increases slightly to a higher value of  $1.2 \times 10^6/l$  during the remaining part of the test. Figure 5 shows the normalized particle size distribution over the whole test duration. Apparently, the proportion of particles in the size range from 6 to 50 nm for the case of 1.2 m/s is way higher than that for a 3.4 m/s sliding velocity. Moreover, the dominating size is shifted from 200 to 150 nm when the sliding velocity is increased from 1.2 to 3.4 m/s.

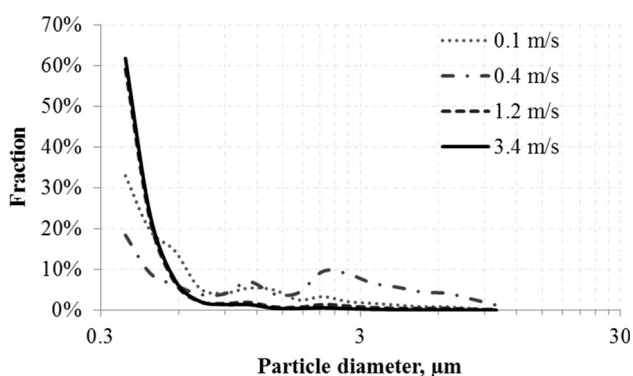


**Fig. 3** Normalized particle size distribution measured by the OPS instrument for the whole test periods for different sliding velocities

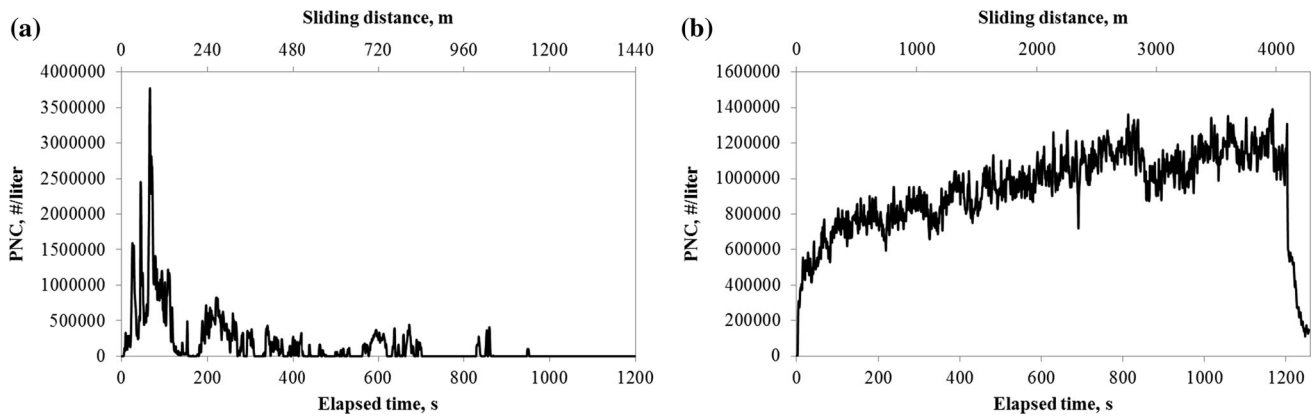
### 3.2 Wear Rate

Figure 6 presents the variation of the wear rate of the tested pins for four studied sliding velocities, namely 0.1, 0.4, 1.2 and 3.4 m/s. Both the mean value and the standard deviation are provided. It can be seen that the pin wear rate increases as the sliding velocity increases from 0.1 to 0.4 m/s, while it clearly drops when the sliding velocity rises from 0.4 to 3.4 m/s. Also, there is a large scatter of the wear rate for the case with a sliding velocity of 0.4 m/s. The maximum peak ( $71.4 \mu\text{g/m}$ ) and the minimum peak ( $3.2 \mu\text{g/m}$ ) of the wear rate appear at a sliding velocity of 0.4 and 3.4 m/s, respectively. More specifically, the average wear rate for a sliding velocity of 0.4 m/s is approximately 24 times higher than that of a 3.4 m/s sliding velocity.

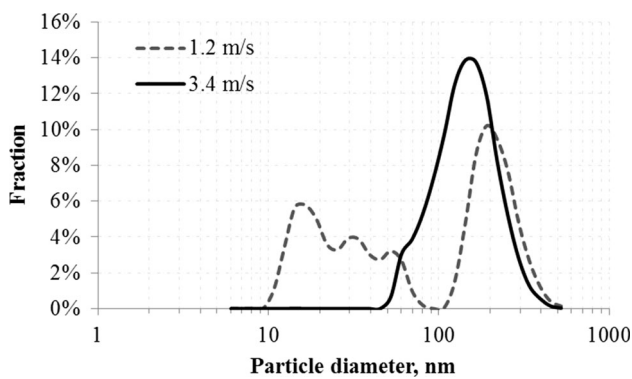
### 3.3 Contact Temperature

Figure 7 shows the measured average contact temperature for three sliding velocities (0.4, 1.2 and 3.4 m/s) over the same sliding distance of 480 m. No measurement was carried out for the case of 0.1 m/s, since only a small temperature increment can be expected. It can be seen that these tests experienced similar variations in temperature. Specifically, a rapid rise took place during the initial stage. Thereafter, a slight increase was detected as the sliding distance is being extended. It should be noted that no insulator was used to avoid the heat losses. Therefore, the measured contact temperature was underestimated to a certain extent. The temperature was up to 27.8, 34.5 and  $57.5 \text{ }^\circ\text{C}$  for sliding velocities of 0.4, 1.2 and 3.4 m/s, at a sliding distance of 480 m, respectively. In order to determine the effect of the temperature variation on the fine and ultrafine particles generation in a case of high sliding velocities (1.2 and 3.4 m/s), the averaged PNC value of the different sliding distance intervals from the FMPS measurements is plotted together with the temperature curve in Fig. 8. As shown in Fig. 8a, the selected test duration (0–318 s corresponding to a sliding distance 0–381.6 m) for the case of a 1.2 m/s sliding velocity was divided into three sliding intervals (SIs). This division was depended on the temperature variation. Specifically, SI 1, SI 2 and SI 3 depict the three temperature variation stages, namely the rapid rise, the slight growth and the steady state, respectively. Also, the three sliding intervals can be related to the variation of the PNC value in Fig. 4a. Apparently, there was a distinct particle size distribution for SI 1, 2 and 3. To be specific, only ultrafine particles were observed during the beginning sliding stage, SI 1 (0–92.4 m), and the corresponding predominant size was around 20 nm. Thereafter, a bimodal PNC distribution with components of both ultrafine and fine particles occurred over an extension of a





**Fig. 4** Particle number concentrations measured by the FMPS instrument under different sliding velocities, **a** 1.2 m/s and **b** 3.4 m/s



**Fig. 5** Normalized particle size distribution measured by the FMPS instrument for the whole test periods for sliding velocities of 1.2 and 3.4 m/s

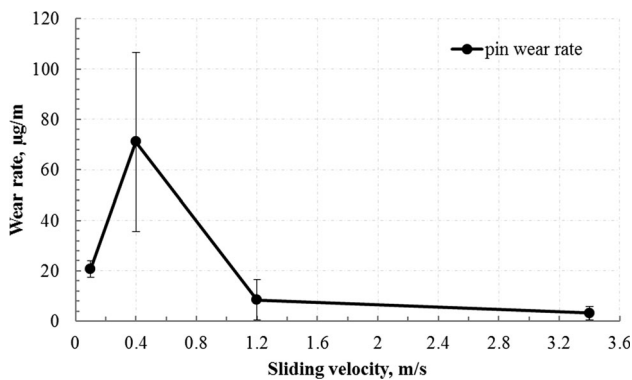


**Fig. 6** Mean wear rate and the relevant standard deviation of tested pins for the following sliding velocities: 0.1, 0.4, 1.2 and 3.4 m/s

sliding distance from SI 1 to SI 2 (92.4–258 m). One main peak was found around 20 nm, while a secondary main peak appeared around 200 nm. Subsequently, fine particles dominated the PNC distribution, while the proportion of ultrafine particles vanished for the following sliding distances: SI 3 (258–381.6 m). Likewise, the PNC level

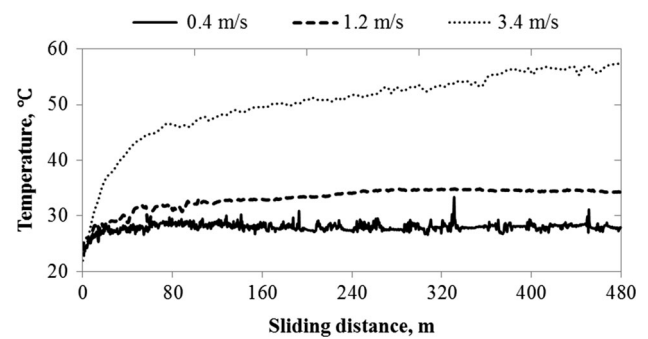


**Fig. 7** Variation of the contact temperature over a sliding distance of 480 m for tests with the following sliding velocities: 0.4, 1.2 and 3.4 m/s

variation was related to the contact temperature measurement during the overall sliding distance (0–1200 s with respect to a sliding distance 0–4080 m) for a sliding velocity of 3.4 m/s (as illustrated in Fig. 8b). According to the temperature variation, the whole test duration was split into three time intervals, SI: 1, 2 and 3 which represents the rapid rise, the slight drop and the fluctuated steady state. Contradictory to what was found in the case of a 1.2 m/s sliding velocity, a similar normal PNC distribution was obtained for all three sliding distance intervals. The particle generation consisted of both ultrafine and fine particles, while the predominant size was found to be around 150 nm.

### 3.4 Pin Worn Surfaces and Airborne Wear Particles

The morphologies of pin worn surfaces identified after the completions of the tests are different for studied sliding velocities. Figure 9 exhibits representative SEM images taken of the pin sample. Also, the inset images of the full view pin worn surface are shown in the figure. As shown in Fig. 9a, b, a rough worn surface was formed for sliding

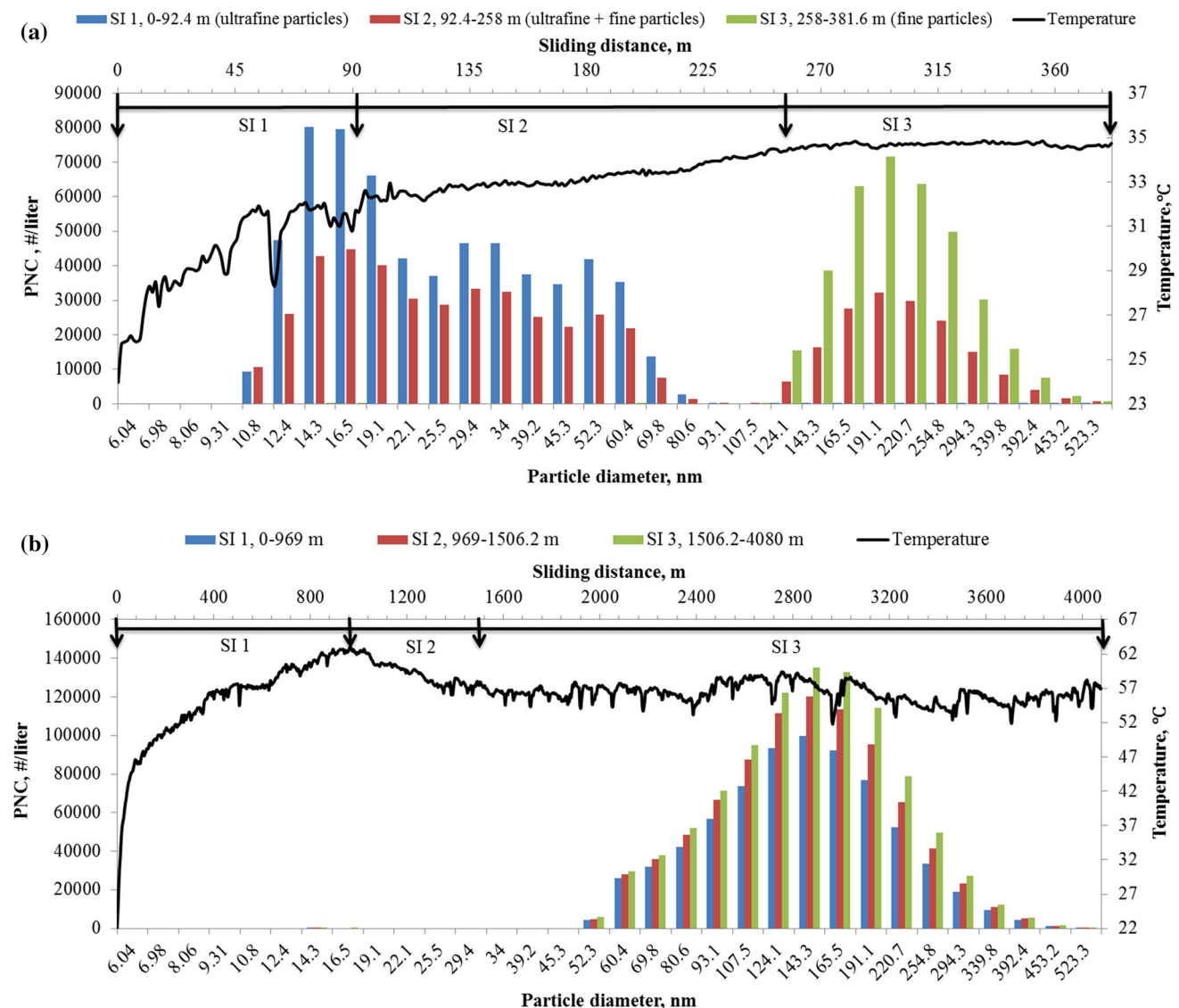


**Fig. 8** Correlation between the contact temperature and the averaged PNC value measured by the FMPS instrument, **a** 1.2 m/s and **b** 3.4 m/s

velocities of 0.1 and 0.4 m/s. A typical abrasive wear characterized by an apparent plowing was detected for the pin worn surfaces for sliding velocities of 0.1 and 0.4 m/s. The corresponding surface deformations were in form of longitudinal grooves parallel to the sliding direction (as pointed out in Fig. 9a, b). Also, the surface delamination indicated that an adhesive wear had taken place. Moreover, a rather large contact area of the pin worn surface was detected for the case of 0.4 m/s (around 4 times larger than for other sliding velocities). For pins tested at high sliding velocities of 1.2 and 3.4 m/s, the worn surfaces were much smoother. Despite that a small scale of abrasive signs can also be seen on the surface, such as a delamination (as pointed out in Fig. 9c) and milder scorings (as pointed out in Fig. 9d), the surface deformation was much milder than for the tests using lower sliding velocities (0.1 and 0.4 m/s).

A further morphology analysis of pin worn surfaces for different sliding velocities (0.4, 1.2 and 3.4 m/s) demonstrated a formation of oxide layers. Figure 10a, b, c shows the full view of these oxide layers within the pin worn surfaces. The images taken at high magnifications which correspond to some certain oxidized areas are presented in Fig. 10d, e, f. All images in Fig. 10 are made by using the SEM-BSE mode. The regions occupied by a relative dark color are determined as the active oxidized areas according to the EDS analysis. The sampling points for the EDS determinations are marked as stars in Fig. 10d, e, f. The average weight percentage (wt%) values of the iron, oxygen, silicon and manganese traces for the sampling points are 74.10, 25.01, 0.26, 0.63; 73.43, 25.06, 0.44, 1.07; 66.21, 33.04, 0.23 and 0.52 % for sliding velocities of 0.4, 1.2 and 3.4 m/s, respectively. Also, the observations show

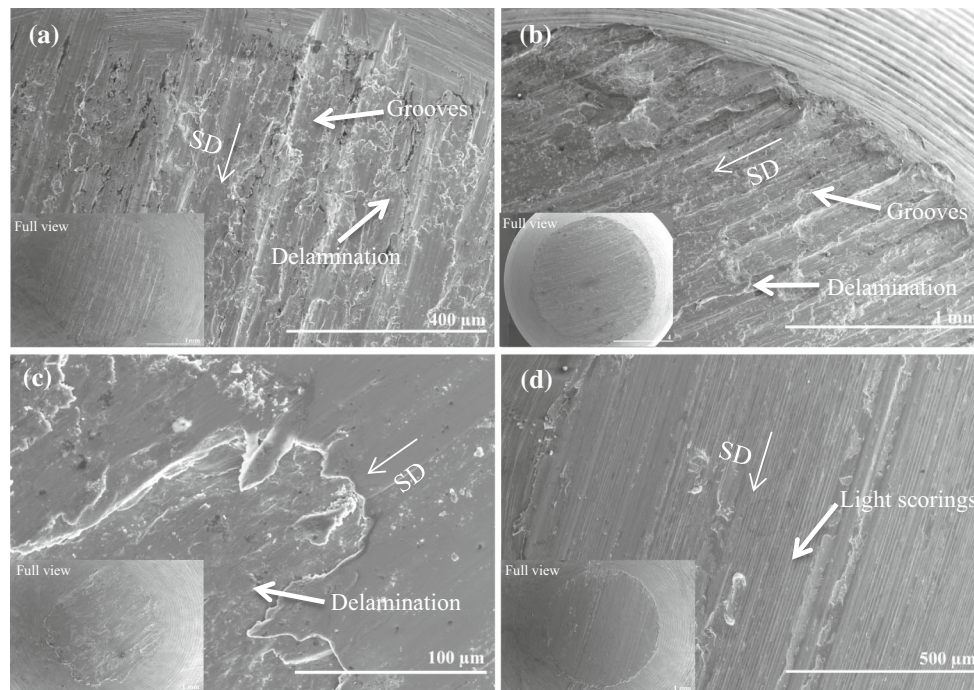


**Fig. 9** SEM micrographs of pin worn surfaces for the following sliding velocities: **a** 0.1 m/s, **b** 0.4 m/s, **c** 1.2 m/s and **d** 3.4 m/s

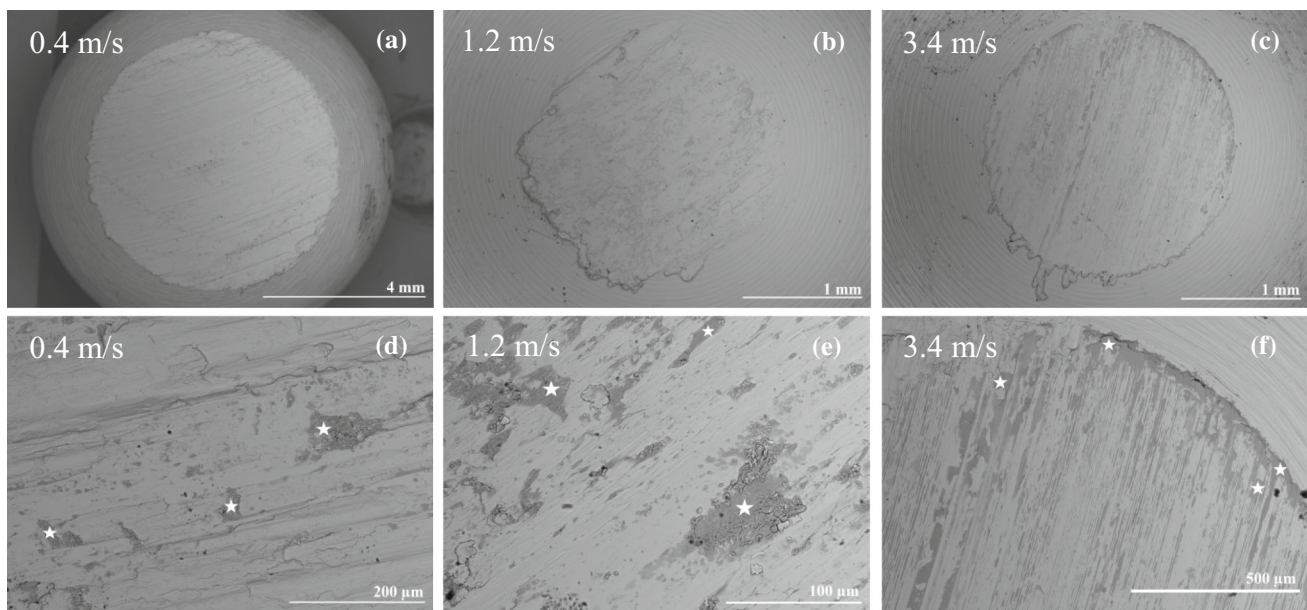


**Fig. 10** SEM micrographs of pin worn surfaces in the BSE modes for following velocities: 0.4 m/s (**a, d**), 1.2 m/s (**b, e**) and 3.4 m/s (**c, f**). In addition, the *star marks* in **d, e** and **f** represent the sampling points used for the EDS composition determinations

that oxide layers tend to appear in small patches along the wear tracks and that they have an irregular shape. Moreover, it is noticeable that the active areas of the oxide layers become larger within the pin worn surface with an increased sliding velocity.

SEM graphs relevant for the characteristics of collected particles are shown in Figs. 11, 12, 13 and 14. Figure 11

shows overview images of the collected particles on the filter of stage 8 ( $D = 510$  nm) for the case of a 1.2 m/s sliding velocity. From left to right, the SEM images were displayed with an increased magnification (150 $\times$ , 1000 $\times$ , 3000 $\times$  and 5000 $\times$ ). The main information extracted from these images is that abundant fine particles were collected and that they could very easily be agglomerated together as



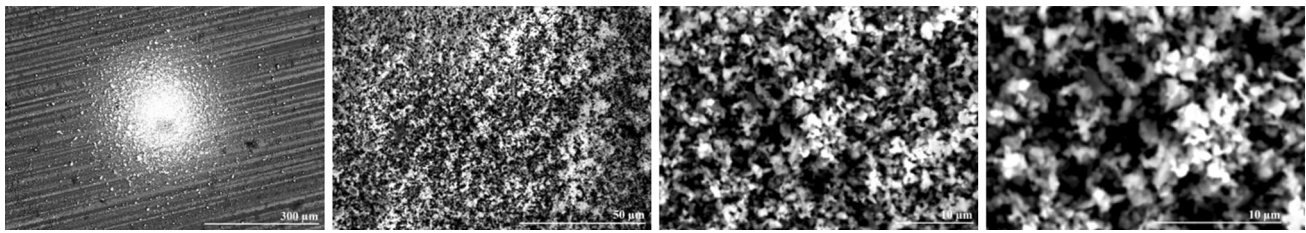


**Fig. 11** SEM images of collected particles on the filter of stage 8 ( $D = 510$  nm) of ELPI+ instrument from the test with a sliding velocity of 1.2 m/s. Data are presented for different magnifications (150 $\times$ , 1000 $\times$ , 3000 $\times$ , 5000 $\times$  from the *left-hand side* to the *right-hand side*)

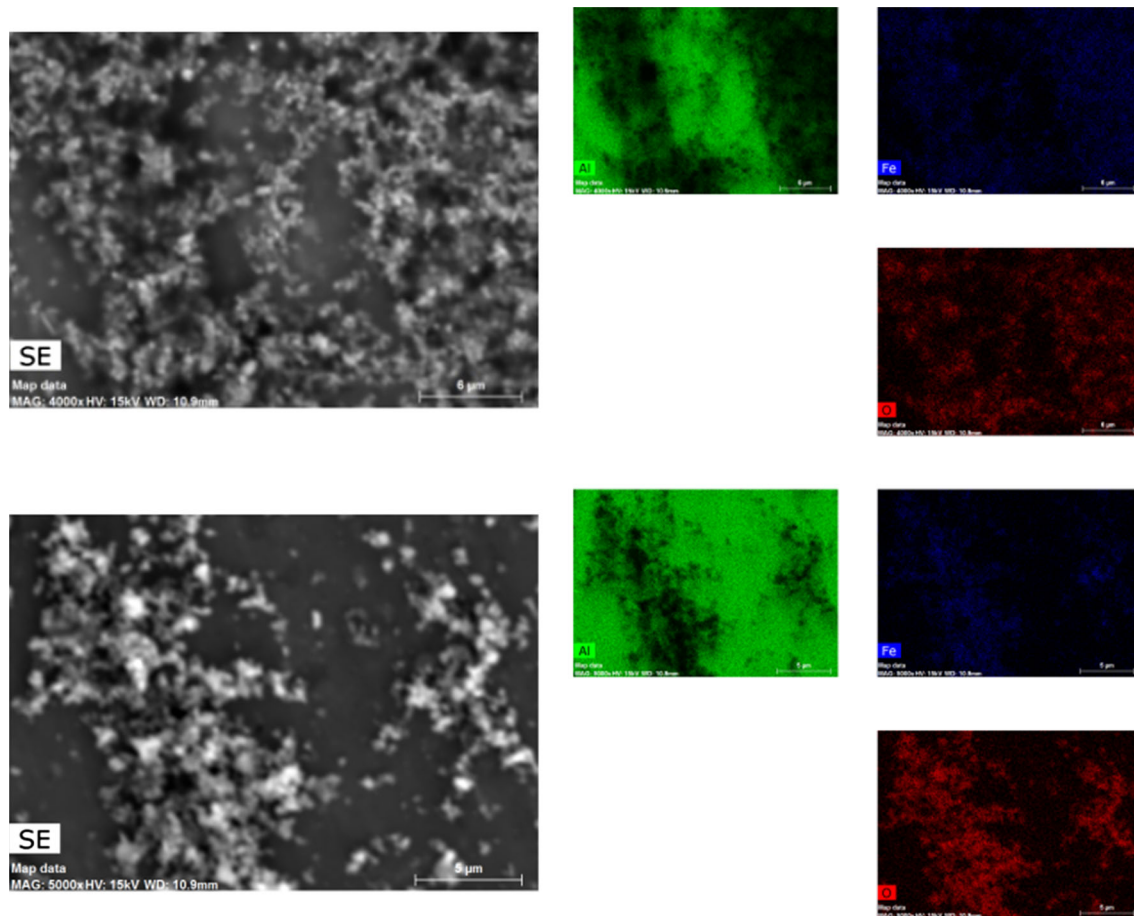


**Fig. 12** SEM elemental mapping data of collected particles on the filter of stage 6 ( $D = 210$  nm) of the ELPI+ instrument from the test with a sliding velocity of 1.2 m/s

clusters on the filter. In Fig. 12, the elemental mapping data of the collected particles on the filter of stage 6 ( $D = 210$  nm) for a 1.2 m/s sliding velocity are illustrated. It should be noted that the area occupied by the trace of aluminum represents a clean aluminum filter without covered particles (as shown in the Al mapping graphs). The presence of the iron and oxygen traces was clearly detected for all collected particles. The homogeneous distribution of iron and oxygen trace reveals that most of the collected particles existed was iron oxide particles. Figures 13

and 14 display the morphology of ultrafine particles collected on the filter of stage 4 ( $D = 80$  nm) and on the filter of stage 2 ( $D = 22$  nm) from a test of 3.4 m/s. The SEM images on the right-hand side in Fig. 13 indicate that some individual ultrafine particles have a round shape. Moreover, a clustering of some ultrafine particles with a diameter of around 1  $\mu$ m had taken place. The characteristics of the collected ultrafine particles on the filter of stage 2 show a similar appearance to those found on the filter of stage 4 (Fig. 13). Some ultrafine particle clusters with a diameter

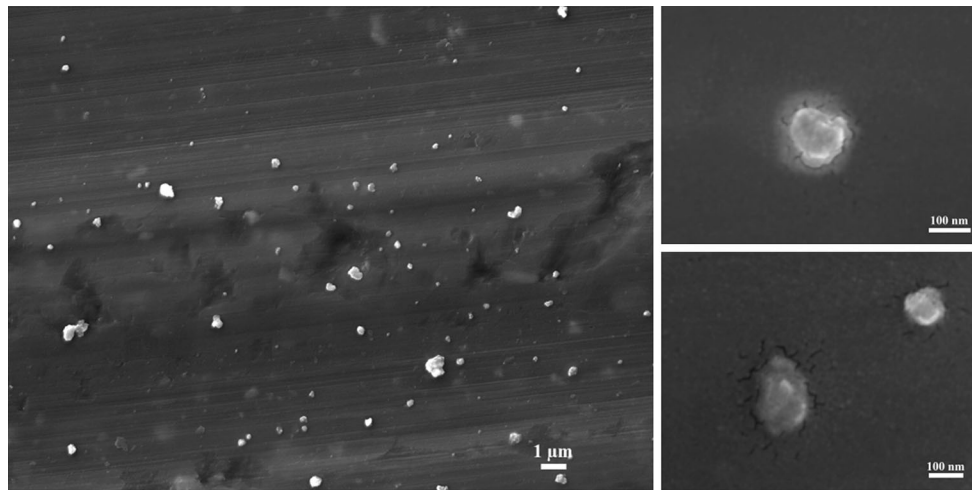


**Fig. 13** SEM images of collected particles on the filter of stage 4 ( $D = 80$  nm) of the ELPI+ instrument from the test with a sliding velocity of 3.4 m/s

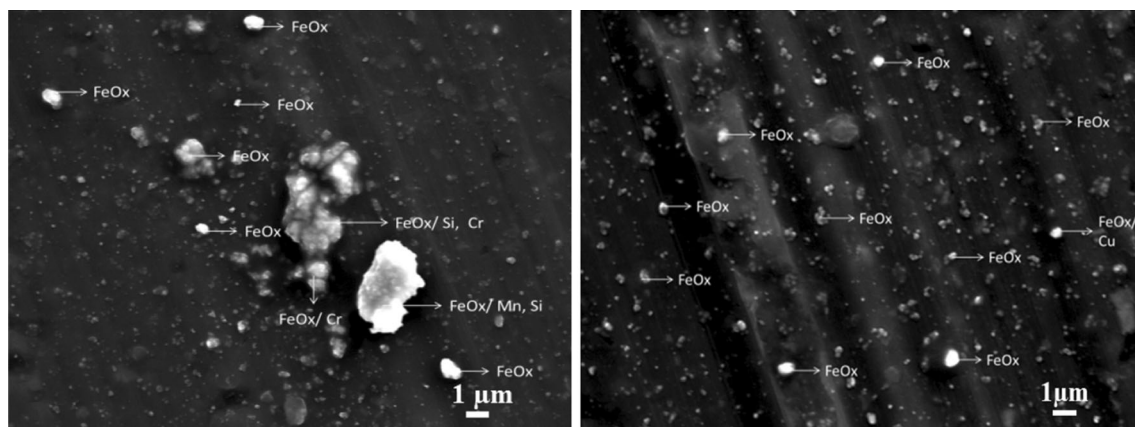


**Fig. 14** Topography and chemical compositions of collected particles on the filter of stage 2 ( $D = 22$  nm) of the ELPI + instrument from the test with a sliding velocity of 3.4 m/s

around 1  $\mu\text{m}$  or larger were selected as representative sample particles for the EDS analysis. This is due to that the resolution of the EDS analysis (the electron beam size) is around 1  $\mu\text{m}$ . The EDS spectra shows that all sampled particles existed in the form of iron oxide particles. Moreover, traces of some other metal elements, such as silicon, manganese and chromium, could also be found in some particles.

#### 4 Discussion

The prior results show that the sliding velocity in a dry sliding wheel–rail contact is a key factor which truly affects the wear rate and the particle emission. A comparison of the PNC value by OPS indicates that the amount of the generated particles increases as a function of the

sliding velocity (Fig. 2). The value of PNC for the case of a 3.4 m/s velocity is approximately 20 times greater than those obtained for sliding velocities of 0.4 and 1.2 m/s. Moreover, even 400 times larger than the value found for a 0.1 m/s sliding velocity. It is also of interest to note that a larger proportion of fine particles are observed for the high sliding velocity cases of 1.2 and 3.4 m/s compared to the low sliding velocity cases of 0.1 and 0.4 m/s (Fig. 3). According to Sundh et al. [5], this distinction can be attributed to that different wear modes are initiated by different sliding velocities. Also, the rapid change of the PNC value observed for a sliding velocity case of 0.4 m/s (Fig. 2b) could be attributed to a possible wear transition. As indicated by the results in Fig. 6, the wear rate of the pins obtained for the cases with low sliding velocities (0.1 and 0.4 m/s) is higher than for the cases with high sliding velocities (1.2 and 3.4 m/s). This obtained variation of the

wear rate with the sliding velocity is in accordance with reported results from a previous study [20]. Moreover, the wear rate results might be attributed to that T1 and T2 wear regime transitions take place for steels when the sliding velocity is increased [21–23]. To be specific, a first transition from mild to severe wear occurs at a critical low sliding velocity (around 0.4 m/s). This could be the reason to the observed unstable wear rate results for a sliding velocity case of 0.4 m/s (Fig. 6). Another transition from severe to mild wear takes place at a critical high sliding velocity (around 1.2 m/s). Also, they are in agreement with the wear appearance observed within the pin worn surface (Figs. 9, 10). A summary of the main wear mechanisms for the tested pin samples with different sliding velocities is listed in Table 4. As shown in Fig. 9a, b, a combination of abrasive and adhesive features was identified for the worn surface at low sliding velocities (0.1 and 0.4 m/s). This causes a rapid material loss, i.e., a high wear rate. This is especially noted for the test with a sliding velocity of 0.4 m/s. To be specific, a continued plowing process cuts more materials off from the mating pin and eventually results in a large contact area (Fig. 9b). Owing to that, more coarse particles and less fine particles were produced in comparison with the cases with high sliding velocities (1.2 and 3.4 m/s). With an increased sliding velocity of 1.2 and 3.4 m/s, a much smoother surface, includes oxide layers, was formed (Fig. 10b, c). These newborn iron oxide layers act as a ‘lubricant’ and construct a third-body wear contact on one hand. On the other hand, the high hardness of iron oxide itself increases the wear resistance of the contact asperities. Consequently, the wear rate declines and a massive of small wear particles are released from the breakdown of the oxide layers.

The FMPS measurement results show that a substantial number of the ultrafine and fine particles are released for the high sliding velocity cases of 1.2 and 3.4 m/s (Fig. 4). A plausible generation mechanism for these substantial ultrafine and fine particles could be a thermal or chemical process rather than a mechanical process [8]. On count of this, the contact temperature is speculated to play a key role for the particle generation. As mentioned in methodology section, the contact temperature was measured by inserting a thermal couple wire into the pin. Thus, it is a measurement of the bulk temperature close to the contact interface rather than a

measurement of the actual contact temperature or the flash temperature. To some extent, this leads to an underestimation of the temperature. This is due to that the produced friction heat from the sliding contact is dissipated into the large sized disk ( $D = 105$  mm) and into the pin holder. To diminish such deviation, a pin holder made of materials with a good thermal insulation property and a smaller disk could be considered in future tests. However, the present temperature measurement method can be used in the current study, since the focus of the study is a comparison between cases with different sliding velocities. The results in Fig. 7 show that the current approach gives a logical trend of the temperature increment.

When relating the temperature variation to the PNC variation for the case of a 1.2 m/s sliding velocity, three particle generation modes, namely ultrafine, ultrafine+ fine and fine particles, are observed for the selected sliding distance intervals: SI 1, 2 and 3 (Fig. 8a), respectively. In SI 1, which represents the initial sliding stage of the test, a sharp rise of the temperature in the pin-disk contact interface leads to the formation of thin oxide layers at certain contact asperities. However, these newborn thin layers are brittle. This results in that within a short lifetime, the layers are subjected to the progress of an alternating destruction and regrowth. As a result, they detach from the parent surface as small wear particles. Therefore, it is very likely that a substantial amount of ultrafine particles are produced from this periodic process during the initial stage of the experiment. Subsequently, the temperature rises slightly in SI 2 and reaches an almost steady-state condition in SI 3 and afterward. Also, the oxide layer becomes thicker, and the removal rate of the oxide layers declines as the experiment proceeds. As a result, the generation of ultrafine and fine particles coexists as a bimodal mode distribution in SI 2, while only fine particles are produced in SI 3. However, it is interesting to note that a homogeneous particle generation mode (the coexistence of ultrafine and fine particles) is observed for the entire test for the case of a 3.4 m/s sliding velocity (Fig. 8b). An explanation can be that a rather high sliding velocity of 3.4 m/s yields a considerable high frictional temperature and promotes the formation of oxide layers in a rapid and sustained manner. Then, the metal–metal contact is quickly substituted by the contact between intact oxide layers, which results in a

**Table 4** Summary of main wear mechanisms which can be identified for the tested sliding wheel rail contacts

Sliding velocity (m/s)	Wear mechanism	Characteristics of pin worn surfaces
0.1	Abrasive + adhesive	Plowing grooves, delamination
0.4	Abrasive + adhesive	Plowing grooves, delamination, a spot of oxide layers
1.2	Oxidative	Oxide layers, delamination
3.4	Oxidative	Plenty of oxide layers, light scorings



stable particle generation mode along with an increase in the total particle number concentration [24].

From the above discussion, one can infer that an oxidative wear is the most likely generation mechanism of the substantial ultrafine and fine particles in a high-speed wheel–rail sliding contact (1.2 and 3.4 m/s). Typically, an oxidative wear is the wear that occurs in a dry unlubricated metal–metal contact in the presence of air or oxygen [25]. In this study, the air is taken from the room which supplies an oxygen atmosphere for all the dry wheel–rail sliding contact tests. These test conditions meet the criteria of an oxidative wear. Moreover, the characteristic features of an oxidative wear are the presence of smooth worn surfaces and small oxidized wear debris [26]. These features are consistent with the SEM observations that are presented in Fig. 10e, f (smooth worn surfaces combined with oxide layers) and in Figs. 11, 12, 13 and 14 (an abundance of iron oxide-containing particles). As pointed out by Quinn [27], the surface flash temperature in a sliding steel–steel contact can be as high as several hundred degrees Celsius at high sliding velocities ( $>1$  m/s). It is also reported that the flash temperature can reach a value of  $750^{\circ}\text{C}$  in a dry sliding wheel–rail contact when the sliding velocity is 0.9 m/s [1]. Therefore, thin oxide layers can build up rapidly in the contact interface. They are fragile and collapse easily, which results in an oxidative wear process. However, few oxide layers are also detected on the pin worn surface for a low sliding velocity of 0.4 m/s (Fig. 10d). It might be explained by the fact that the low sliding velocity is unable to yield a high enough friction temperature. Thus, this can hardly cause a direct oxidation. Instead, the formation of those oxide layers seems to be a consequence of the mechanical behavior in the contact surface rather than due to a thermal effect [28]. According to above evidences, it is indicated that massive ultrafine and fine particles are produced by oxidative wear processes during a high-speed sliding wheel–rail contact. Furthermore, it is interesting to note that substantial ultrafine and fine particles are generated for a sliding velocity around the assumed T2 wear regime transition point (1.2 m/s) and after it as well (3.4 m/s). Therefore, an investigation should be carried out to study if there is a correlation between the T2 transition and the particle generation. This work might provide a new perspective to understand the different particle generation mode in a dry sliding wheel–rail contact. More tests are needed to be done. However, this is deemed to be out of the focus of the present study.

If we scale up the pin-on-disk test results to wheel–rail contact conditions, one can see that the amount of the relative sliding velocity in the rolling sliding wheel–rail contact will influence the amount of wear and the generation of airborne particulates significantly. Especially, the wheel–rail contact under high sliding velocities (a heavy

brake in a sharp curve) could produce an abundant emission of iron oxide-containing airborne particulates in the fine and ultrafine size ranges. This indicates that it, for instance, can be beneficial to avoid braking in narrow curves in tunnel environments, which is a situation where relative high sliding velocities are generated. Moreover, even some typical wheel–rail contact conditions with a sliding velocity of 0.4 m/s (a rail gauge–wheel flange contact) were found to be able to trigger a severe wear as well as a high wear rate. This might result in an inevitable material loss of the wheel and the rail, and it can cause safety issues with respect to the stability of the wheel–rail contact. Further research concerning the particulate emissions when a heavy acceleration or braking takes place in sharp curves could facilitate a better understanding of the generation of particles due to a wheel–rail contact.

## 5 Conclusion

Pin-on-disk tests were used to investigate how the sliding velocity influences the particle generation in a dry sliding wheel–rail contact under controlled contact conditions. The particle number concentration and size distribution, the wear rate, the average contact temperature together with morphological and chemical characteristics of pin worn surfaces and the collected particles were examined. The following main conclusions can be drawn from the results of this study:

- In a dry sliding wheel–rail contact, the sliding velocity significantly influences the particles generation in terms of the particle number concentration and size distribution. Specifically, the particle number concentration level increases remarkably with an increased sliding velocity. Also, a high-speed sliding wheel–rail contact (1.2 and 3.4 m/s) can produce an abundance of particles (millions per liter) in the ultrafine and fine size ranges.
- With a low sliding velocity of 0.1 and 0.4 m/s, the wheel–rail contact undergoes a combination of abrasive and adhesive wear and the wear rate is high. Furthermore, an oxidative wear is prevailed and subjected to the wheel–rail contact when a high sliding velocity of 1.2 and 3.4 m/s is conducted. The formation of oxide layers effectively prevents the pins from a severe wear, i.e., the wear rate is low.
- The average contact temperature variation is strongly related to the different particle generation modes of a sliding wheel–rail contact at high sliding velocities (1.2 and 3.4 m/s).
- The present work reveals that a substantial number of ultrafine and fine particles are mainly generated from an



oxidative wear process in a wheel–rail contact under high sliding velocities (1.2 and 3.4 m/s).

**Acknowledgments** The authors Hailong Liu and Yingying Cha wish to acknowledge the financial supports by the China Scholarship Council (CSC).

**Open Access** This article is distributed under the terms of the Creative Commons Attribution 4.0 International License (<http://creativecommons.org/licenses/by/4.0/>), which permits unrestricted use, distribution, and reproduction in any medium, provided you give appropriate credit to the original author(s) and the source, provide a link to the Creative Commons license, and indicate if changes were made.

## References

- Lewis, R., Olofsson, U.: Mapping rail wear regimes and transitions. *Wear* **257**, 721–729 (2004)
- Gustafsson, M.: Airborne particles from the wheel–rail contact. In: Lewis, R., Olofsson, U. (eds.) *Wheel–Rail Interface Handbook*, pp. 550–575. CRC Press LLC, Florida (2009)
- Abbasi, S., Jansson, A., Sellgren, U., Olofsson, U.: Particle emissions from rail traffic: a literature review. *Crit. Rev. Environ. Sci. Tech.* **43**, 2511–2544 (2013)
- Braniš, M.: The contribution of ambient sources to particulate pollution in spaces and trains of the Prague underground transport system. *Atmos. Environ.* **40**, 348–356 (2006)
- Sundh, J., Olofsson, U., Olander, L., Jansson, A.: Wear rate testing in relation to airborne particles generated in a wheel–rail contact. *Lubr. Sci.* **21**, 135–150 (2009)
- Sundh, J., Olofsson, U.: Relating contact temperature and wear transitions in a wheel–rail contact. *Wear* **271**, 78–85 (2011)
- Abbasi, S., Olofsson, U., Zhu, Y., Sellgren, U.: Pin-on-disc study of the effects of railway friction modifiers on airborne wear particles from wheel–rail contacts. *Tribol. Int.* **60**, 136–139 (2013)
- Olofsson, U., Zhu, Y., Abbasi, S., Lewis, R., Lewis, S.: Tribology of the wheel–rail contact—aspects of wear, particle emission and adhesion. *Veh. Syst. Dyn.* **51**, 1091–1120 (2013)
- Zimmer, A.T., Maynard, A.D.: Investigation of the aerosols produced by a high-speed, hand-held grinder using various substrates. *Ann. Occup. Hyg.* **46**, 663–672 (2012)
- Suzumura, J., Sone, Y., Ishizaki, A., Yamashita, D., Nakajima, Y., Ishida, M.: In situ X-ray analytical study on the alteration process of iron oxide layers at the railhead surface while under railway traffic. *Wear* **271**, 47–53 (2011)
- Zhu, Y., Olofsson, U., Chen, H.: Friction between wheel and rail: a pin-on-disc study of environmental conditions and iron oxides. *Tribol. Lett.* **52**, 327–339 (2013)
- Nemmar, A., Vanbilloen, H., Hoylaerts, M.F., Hoet, P.H.M., Verbruggen, A., Nemery, B.: Passage of intratracheally instilled ultrafine particles from the lung into the systemic circulation in hamster. *Am. J. Respir. Crit. Care Med.* **164**, 1665–1668 (2001)
- Dick, C.A.J., Brown, D.M., Donaldson, K., Stone, V.: The role of free radicals in the toxic and inflammatory effects of four different ultrafine particle types. *Inhal. Toxicol.* **15**, 39–52 (2003)
- Knibbs, L.D., Cole-Hunter, T., Morawska, L.: A review of commuter exposure to ultrafine particles and its health effects. *Atmos. Environ.* **45**, 2611–2622 (2011)
- Olofsson, U., Olander, L., Jansson, A.: A study of airborne wear particles generated from a sliding contact. *J. Tribol.* **131**, 044503 (2009)
- Sundh, J., Olofsson, U., Sundvall, K.: Seizure and wear rate testing of wheel–rail contacts under lubricated conditions using pin-on-disc methodology. *Wear* **265**, 1425–1430 (2008)
- Kumar, P., Fennell, P., Symonds, J., Britter, R.: Treatment of losses of ultrafine aerosol particles in long sampling tubes during ambient measurements. *Atmos. Environ.* **42**, 8819–8826 (2008)
- Greenwood, J.A., Williamson, J.B.P.: Contact of nominally flat surfaces. *Proc. R. Soc. Lond. A Math. Phys. Eng. Sci.* **295**, 300–319 (1966)
- Olofsson, U., Olander, L., Jansson, A.: Towards a model for the number of airborne particles generated from a sliding contact. *Wear* **267**, 2252–2256 (2009)
- Olofsson, U., Telliskivi, T.: Wear, plastic deformation and friction of two rail steels—a full-scale test and a laboratory study. *Wear* **254**, 80–93 (2003)
- Welsh, N.C.: The dry wear of steels I. The general pattern of behaviour. *Philos. Trans. R. Soc. Lond. Ser. A* **257**, 31–50 (1965)
- Welsh, N.C.: The dry wear of steels II Interpretation and special features. *Philos. Trans. R. Soc. Lond. Ser. A* **257**, 51–70 (1965)
- Viáfara, C.C., Sinatora, A.: Influence of hardness of the harder body on wear regime transition in a sliding pair of steels. *Wear* **267**, 425–432 (2009)
- Stachowiak, G., Batchelor, A.W.: *Engineering Tribology*. Butterworth-Heinemann, Oxford (2013)
- Quinn, T.F.J.: Review of oxidational wear: part I: the origins of oxidational wear. *Tribol. Int.* **16**, 257–271 (1983)
- Quinn, T.F.J.: Review of oxidational wear part II: recent developments and future trends in oxidational wear research. *Tribol. Int.* **16**, 305–315 (1983)
- Quinn, T.F.J.: Oxidational wear modelling part III. The effects of speed and elevated temperatures. *Wear* **216**, 262–275 (1998)
- Viáfara, C.C., Sinatora, A.: Unlubricated sliding friction and wear of steels: an evaluation of the mechanism responsible for the T1 wear regime transition. *Wear* **271**, 1689–1700 (2011)